X-Ray Radiographic System Used to Measure the Evolution of Broadband Imprint in Laser-Driven Planar Targets

In an inertial confinement fusion (ICF) implosion, the target is hydrodynamically unstable, and, as a result, mass modulations in the target (either existing or created) can grow to be large enough to disrupt the implosion, thereby reducing its thermonuclear yield.[1] In direct-drive ICF, the nonuniformities in the drive laser can create mass modulations in the target by a process called laser imprinting. As the target accelerates, these mass modulations can grow exponentially, creating large perturbations in the target shell. Understanding and controlling laser imprinting are critical to the successful design of a high-gain ICF target. The primary method of studying imprinting is through-foil x-ray radiography of laser-accelerated targets, where the growth of these mass modulations can be observed.[2] Planar targets are used because they are easily diagnosed and are a reasonable approximation to the early portions of a spherical implosion.

Our experiments use multiple laser beams to drive the subject target and to produce x rays on another target.[3] These x rays are filtered and imaged after they traverse the driven target. Modulations in these images are related to the optical depth (or density–thickness product) of the target. By properly interpreting these images, the character of the imprinted features and their temporal evolution are studied. To accomplish this, the instrumentation must be properly characterized.

A direct measurement of the initial imprinted perturbations is difficult because of their low amplitudes. Additional complications result from the propagation effects of nonuniform shock waves.[4–6] Low-amplitude imprinting has been measured directly using an XUV laser to probe target nonuniformities produced by a laser on very thin (~2 to 3 μm) silicon and aluminum targets.[7] The present experiments use 20-μm-thick CH targets that closely resemble the target shells normally used on OMEGA spherical implosions. These experiments are closely related to those that measure the growth of preimposed mass perturbations,[4] which were well simulated by hydrocodes, providing confidence that both the energy coupling and amount of unstable growth are well modeled for these experiments. This provides a baseline calibration for various hydrodynamic effects that occur in the imprinting experiments. A caveat for these experiments is that imprinting is not directly measured; rather, some unstable RT growth is needed to amplify the perturbations to detectable levels.

It should also be noted that the hydrodynamic instabilities studied here exist primarily at the ablation surface, the point where the steep temperature front meets the overdense material produced by the shock. Perturbations in the target result from both mass modulations (ripples on the ablation surface) and density modulations produced in the bulk of the target. The latter are created primarily by the propagation of nonuniform shocks. Radiographic systems are sensitive to the density–thickness product (optical depth) of the target and, as such, cannot distinguish between mass and density modulations. After about 1 ns of acceleration in these experiments, the variations in optical depth produced by the nonuniform shocks become negligible, compared to those produced by the ablation-front amplitude. At this point, it is reasonable to ascribe most of the measured optical depth to the amplitude of the perturbation at the ablation surface.[4]

The backlighting source typically has multiple spectral components. As a result, simulations of the resultant optical depth of the target are critical to interpreting the data. This worked extremely well for experiments using two-dimensional preimposed sinusoidal perturbations.[4,8] In contrast, the features created by imprinting are three dimensional and significantly more difficult to simulate. It is advantageous, therefore, to obtain experimentally a relationship between measured optical-depth modulations and the amplitude of ablation-surface modulations. We simplify the latter process by establishing several reasonable assumptions about the detection system.

In the following sections, we discuss the radiographic imaging system and methods to recover the target perturbations from the radiographs. We present results of experiments that characterize the sensitivity, resolution, and noise of the system. Using this information, we have formulated a Wiener

filter that is designed to enhance the radiographic images. In essence, our analysis provides a way to distinguish signal from noise and to deconvolve the system resolution.

Experimental Configuration

Unperturbed (smooth surface), 20-μm-thick CH (ρ = 1.05 g/cm^3) targets were irradiated at 2×10^{14} W/cm^2 in 3-ns square pulses by five overlapping UV beams (see Fig. 76.33). The targets were backlit with x rays produced by a uranium backlighter, located 9 mm away from the driven target and irradiated at ~1×10^{14} W/cm^2 (using 12 additional beams). X rays transmitted through the target and a 3-μm-thick Al blast shield (located at the center between the backlighter and drive

foils) were imaged by 8-μm pinholes on a framing camera filtered with 6 μm of aluminum. This yielded the highest sensitivity for an average photon energy of ~1.3 keV. The framing camera produced eight images of ~80-ps duration, each occurring at different times. The distance between the target and the pinhole array was 2.5 cm, and the distance between the pinhole array and the framing camera was 35 cm, resulting in a magnification of ~14. The use of optical fiducial pulses coupled with an electronic monitor of the framing-camera output produced a frame-timing precision of about 70 ps. The framing-camera output is captured on Kodak T-Max 3200 film, which is then digitized with a Perkin–Elmer PDS microdensitometer with a 20-μm-square scanning aperture.

Figure 76.34 shows a block diagram of the entire detection system, which comprises four major parts: an 8-μm pinhole, the framing camera with a microchannel plate (MCP) and phosphor plate, the film, and the digitization process. At each stage of the measurement, noise is added to the signal, and the signal plus noise are convolved with the point spread function (PSF) of each component of the system. In the frequency domain, the spectra of both the signal and the noise are multiplied by a modulation transfer function (MTF) of that subset of the imaging system.

In radiography, x rays with a nominally wide spectrum are attenuated exponentially by the target being probed. In addition to the target, there are filters and imaging devices that affect the transmission of x rays to the detector. Figure 76.35 (thick line) shows a backlighter uranium spectrum used for imaging.[2] The spectral response function of the imaging system (Fig. 76.35, thin line) includes the transmission of

Figure 76.33

Experimental configuration. Five overlapped beams drive a 20-μm CH foil. An additional 12 beams produce x rays from a uranium backlighter foil. X rays traverse the target and are imaged by a pinhole array on a framing camera.
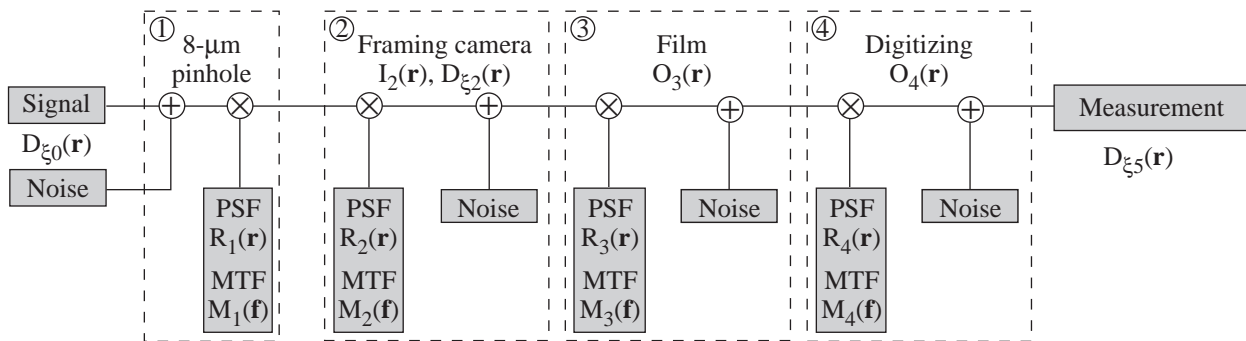
Figure 76.34

Block diagram of the experimental detection system. This system comprises four major parts: an 8-μm pinhole, the framing camera, the film, and the digitization. At each stage of the measurement, noise is added to the signal, and the signal with noise are convolved with the PSF. $D_{\xi 0}(\mathbf{r})$, $D_{\xi 2}(\mathbf{r})$, and $D_{\xi 5}(\mathbf{r})$ are the optical depth modulations in the target, in the framing camera's output, and as measured, respectively. $I_2(\mathbf{r})$ is the light intensity in the framing camera's output. $O_3(\mathbf{r})$ and $O_4(\mathbf{r})$ are the optical density of the film, before and after digitization, respectively.

aluminum filters and mass absorption rate of a gold photocathode on the microchannel plate (MCP) in the framing camera. Figure 76.36 shows the spectrum used for imaging, absorbed and converted into electrons by the MCP. It is obtained by multiplying the two curves in Fig. 76.35 together, taking the attenuation of 20 μm CH into account. The output of the framing camera is proportional to the convolution of the x-ray spectral intensity incident on a target, its attenuation factor, and the PSF's of the pinhole $R_1(\mathbf{r},E,t)$ and the framing camera $R_2(\mathbf{r},E,t)$, including filters, where E represents x-ray energy. Assuming that no saturation occurs in these devices, the output intensity of the framing camera incident on the film is
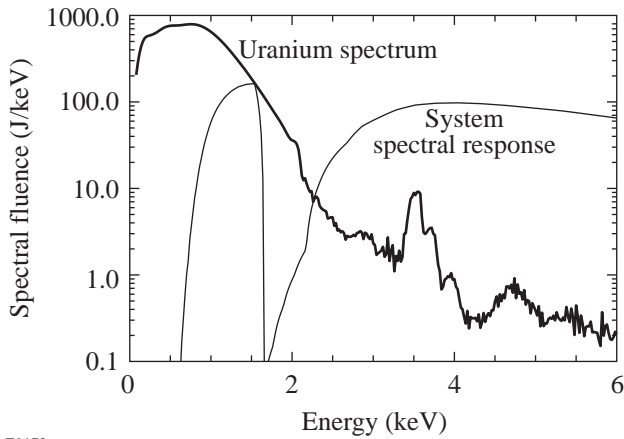
E9172

Figure 76.35
Uranium spectrum (thick solid line) and instrumental response (thin solid line) as functions of x-ray energy.
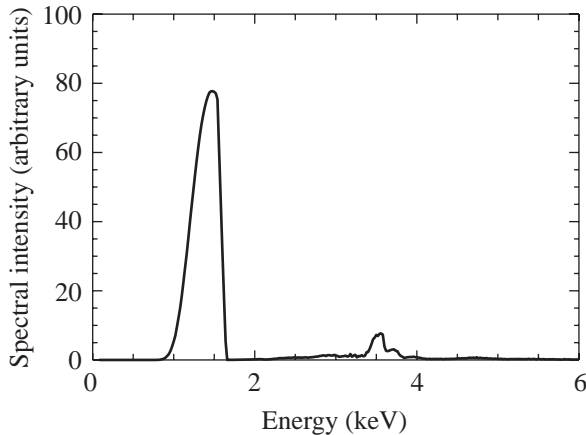
E9183

Figure 76.36
X-ray spectrum propagated through a 3-μm Al blast shield, a 20-μm CH target, and a 6-μm Al filter on the MCP, then absorbed and converted into electrons by the MCP.

$$
\begin{aligned}
I_2(\mathbf{r},t) \sim & \int dE \int d\mathbf{r}' \\
& \times R_{1,2}(\mathbf{r}-\mathbf{r}',E,t)\, f_{\text{Al}}(E,t)\, \mu_{\text{Au}}(E)\, S_{\text{bklt}}(\mathbf{r}',E,t) \\
& \times \exp\!\left[-\int_0^{z_0} dz'\, \mu_{\text{CH}}(E,t)\, \rho(\mathbf{r}',z',t)\right] \\
& \times \exp\!\left[-\mu_{\text{CH}}(E,t)\, \rho_{\text{abl}}(t)\, \xi(\mathbf{r}',t)\right].
\end{aligned}
\tag{1}
$$

In this equation, x rays propagate along the target normal, which is oriented along the z axis. The coordinate $\mathbf{r}$ is the position vector perpendicular to that axis; $I_2(\mathbf{r},t)$ is the output intensity of the framing camera; $R_{1,2}(\mathbf{r},E,t)$ is a point spread function of a pinhole and framing cameras, which is, in general, a function of the x-ray energy E; $f_{\text{Al}}(E,t)$ is the aluminum filter transmission; $\mu_{\text{Au}}(E)$ is the mass absorption rate of the gold photocathode (in the MCP); and $S_{\text{bklt}}(\mathbf{r},E,t)$ is a backlighter spectral intensity. The target density and thickness are $\rho(\mathbf{r},z,t)$ and $z_0(t)$, respectively. The target density and the amplitude of the target thickness modulation at the ablation surface are $\rho_{\text{abl}}(t)$ and $\xi(\mathbf{r},t)$. The mass absorption rate of the CH target is $\mu_{\text{CH}}(E,t)$.

The film converts the incident light intensity $I_2(\mathbf{r},t)$ into the film optical density $O_3(\mathbf{r},t)$ according to its sensitivity [or D log(H)] curve W. Convolving that with the PSF of the film $R_3(\mathbf{r})$ yields

$$
\begin{aligned}
O_3&(\mathbf{r},t) \\
&= \int d\mathbf{r}'\, R_3(\mathbf{r}-\mathbf{r}')\, W\!\left\{\log_{10}\!\left[\int_{t-\tau/2}^{t+\tau/2} dt'\, I_2(\mathbf{r}',t')\right]\right\},
\end{aligned}
\tag{2}
$$

where $\tau = 80$ ps is a time resolution of the framing camera. During film digitization, the optical density $O_3(\mathbf{r},t)$ is convolved with the PSF $R_4(\mathbf{r})$ of the 20-μm-square aperture in the densitometer to give the digitized or measured optical density

$$
O_4(\mathbf{r},t) = \int d\mathbf{r}'\, R_4(\mathbf{r}-\mathbf{r}')\, O_3(\mathbf{r}').
\tag{3}
$$

The measured optical density of the film, $O_4(\mathbf{r},t)$, is converted to intensity using the inverse film sensitivity W^{-1}. The measured optical depth $D_5(\mathbf{r},t)$ of the target is obtained by taking the natural logarithm of that intensity-converted image:

$$
D_5(\mathbf{r},t) = \ln\!\left\{10^{W^{-1}[O_4(\mathbf{r},t)]}\right\}.
\tag{4}
$$

The primary objective of this experiment is to recover the amplitude of the perturbation at the ablation surface using the

measured optical depth modulations. To do this rigorously requires significant effort. Several aspects of the imaging system enable assumptions, however, that greatly simplify the analysis of the radiographic images: (1) As a result of Al filters, a relatively narrow band ($\Delta E \simeq 200\,\mathrm{eV}$) of x rays around 1.3 keV is used for radiography. The effect of the spectral component of uranium M-band emission around 3.5 keV (see Fig. 76.36) on system sensitivity and resolution was measured and calculated to be insignificant. (2) The backlighter spectrum and filter transmission remain constant in time during the measurement. (3) The backlighter is produced by 12 beams that have phase plates, resulting in a very uniform and predictable backlighter shape. (4) There is little heating of the solid part of the target (the mass absorption coefficient μ is constant in time). (5) The amplitudes of growing imprinted features are large enough that the propagation of a nonuniform shock contributes little to the total optical depth of the target.[4] Given these assumptions, Eq. (1) becomes

$$I_2(\mathbf{r},t) \sim I_{\mathrm{env}}(\mathbf{r},t)\int d\mathbf{r}' R_{1,2}(\mathbf{r}-\mathbf{r}')\exp\left[-D_{\xi0}(\mathbf{r}',t)\right], \quad (5)$$

where the modulation in a target optical depth $D_{\xi0}(\mathbf{r},t)$ is simply

$$D_{\xi0}(\mathbf{r},t) = \frac{\xi(\mathbf{r},t)}{\lambda_{\mathrm{CH}}}, \quad (6)$$

and the spectrally weighed attenuation length of the target λ_{CH} is given as

$$\lambda_{\mathrm{CH}} \simeq 1/\left[\mu_{\mathrm{CH}}(1.3\ \mathrm{keV})\rho_{\mathrm{abl}}\right]. \quad (7)$$

$I_{\mathrm{env}}(\mathbf{r},t)$ is the slowly varying envelope of the backlighter.

At this point, the target optical depth can be obtained from the measured optical depth by rigorously working backward through each stage, compensating for noise and system response (PSF) at each stage. However, if the modulation in the target optical density $D_{\xi0}(\mathbf{r},t)$ is small,

$$D_{\xi0}(\mathbf{r},t) \ll 1 \quad (8)$$

(which is the case in all our experiments), the entire imaging system may be considered linear. This greatly simplifies the relation between the measured optical depth and the target optical depth. We introduce a new variable, the optical depth modulation in the output of the framing camera $D_{\xi2}(\mathbf{r},t)$,

through the following equation:

$$I_2(\mathbf{r},t) \sim I_{\mathrm{env}}(\mathbf{r},t)\exp\left[-D_{\xi2}(\mathbf{r},t)\right]. \quad (9)$$

Next, assuming that $D_{\xi0}(\mathbf{r},t)$ and $D_{\xi2}(\mathbf{r},t)$ are small, we expand in Taylor series the exponential functions in Eqs. (5) and (9) and retain only zeroth and first orders in these expansions. We then have

$$D_{\xi2}(\mathbf{r},t) \cong \int d\mathbf{r}' R_{1,2}(\mathbf{r}-\mathbf{r}',t)D_{\xi0}(\mathbf{r}',t). \quad (10)$$

Here we used the fact that the point spread function $R_{1,2}(\mathbf{r},t)$ is normalized $\int d\mathbf{r}\,R_{1,2}(\mathbf{r},t)=1$. The T-MAX 3200 film has a constant MTF up to a spatial frequency ~50 mm^{-1}, the highest spatial frequency considered in our measurements, so the PSF of the film is set to be a $\delta(\mathbf{r})$ function. Since we use only the "linear" part of the $D\log(H)$ curve, the modulations in measured optical depth $D_{\xi5}(\mathbf{r},t)$ are linearly related to the optical depth modulation in the target $D_{\xi0}(\mathbf{r},t)$:

$$D_{\xi5}(\mathbf{r},t) = \int d\mathbf{r}' R_{\mathrm{sys}}(\mathbf{r}-\mathbf{r}')D_{\xi0}(\mathbf{r}',t), \quad (11)$$

where $R_{\mathrm{sys}}(\mathbf{r})$ is the PSF of the entire system. It is the convolution of PSF's of the pinhole, the framing camera, and the digitizing aperture of the densitometer. In frequency space, the system MTF is the product of the MTF's of each of these components.

In summary, we have used approximations of the system performance to find a straightforward relationship between the measured optical depth and the modulation of the ablation surface. As opposed to requiring detailed computer simulations to interpret experimental results, we find, for a class of experiments, a direct relationship between the measurement and target perturbations. Equation (11) has been derived by assuming that modulations of the target optical depth are small compared to unity. Since Eq. (11) is a linear approximation, it does not treat the generation of harmonics and coupling of modes produced by system nonlinearities. We have simulated these nonlinearities for modulation amplitudes greater than those measured routinely in our experiments and found that nonlinear effects were negligible compared to system noise.

System Sensitivity

Once the modulation in target optical depth is obtained (see above), the perturbation amplitude in the target can be found,

provided various criteria are met. Variations in optical depth are produced by changes in either the target density or target thickness. Apparent changes in optical depth can also result from changes in the x-ray spectrum or in the attenuation coefficient of the target material. We performed several experiments to characterize the system performance.

System sensitivity is defined by the spectrally weighted x-ray attenuation length λ_{CH}. This length is inversely proportional to the mass absorption coefficient and the target density [see Eq. (7)]. In practice, λ_{CH} can be constructed using the target compression C_p, calculated by the 1-D hydrocode *LILAC*,[9] and the attenuation length of the undriven target λ_x:

$$\lambda_{CH} = \frac{\lambda_x}{C_p}. \tag{12}$$

This relation can be used as long as the driven target maintains a cold value of its mass absorption coefficient. Typically, during our experiments the target temperature is far below the values that could change the mass absorption coefficient.

We measured the attenuation length λ_x in undriven 25-μm CH$_2$ ($\rho = 0.92$ g/cm^3) targets using backlighter beams only. At the position of the experimental target, a thin strip of CH$_2$ was mounted so that the radiographic system could view x rays that both miss and traverse the target, as shown on the image taken at some time during the 3-ns backlighter pulse [see Fig. 76.37(a)]. The calculated attenuation length for this material was 11.5 μm, and we measured 10 μm±1 μm from the difference in optical depth in these two regions [lines A and B in Fig. 76.37(b)]. This value was constant for the ~1-mm backlighter spot and did not vary over the duration of the 3-ns backlighter pulse. We also radiographed undriven 20-μm CH ($\rho = 1.05$ g/cm^3) targets that had preimposed, low-amplitude (0.5 μm) sinusoidal modulations with wavelengths of 60 and 30 μm. Using these modulations as control references, λ_x was measured to be 10 μm±2 μm. These experiments showed that both backlighter spectrum and filter transmission remained constant in time during the measurements.

System Resolution

The resolution of the system was characterized by measuring its response to a sharp, opaque edge (machined platinum). Its image is shown in Fig. 76.38(a). The dashed line in Fig. 76.38(b) represents the light intensity incident on the edge, the thin solid line is the measured light intensity propagated through the system (and averaged in the direction parallel to the edge), and the thick solid line is the fit to experimental

data assuming the system MTF as a two-Gaussian function:[10]

$$M_{sys}(f) = 0.955 \exp\left\{-\left[14.2\,(\mu m)f\right]^2\right\}$$
$$+ 0.045 \exp\left\{-\left[248.3\,(\mu m)f\right]^2\right\}. \tag{13}$$

The MTF is essentially the product of the responses of three system components: the pinhole camera, the 20-μm digitizing aperture, and the framing camera. The former two are straightforward calculations based on geometry and spectral energy. The MTF of the framing camera was determined by measuring the camera response to a 150-μm-wide slit (placed 1 mm in front of the camera) backlit by x rays [see Fig. 76.39(a)]. This image of the slit was digitized with a 5-μm scanning aperture. The slit width and its proximity to a camera were sufficient to neglect any diffraction effects. The dashed line in Fig. 76.39(b) represents the light intensity incident on the slit. The thin solid
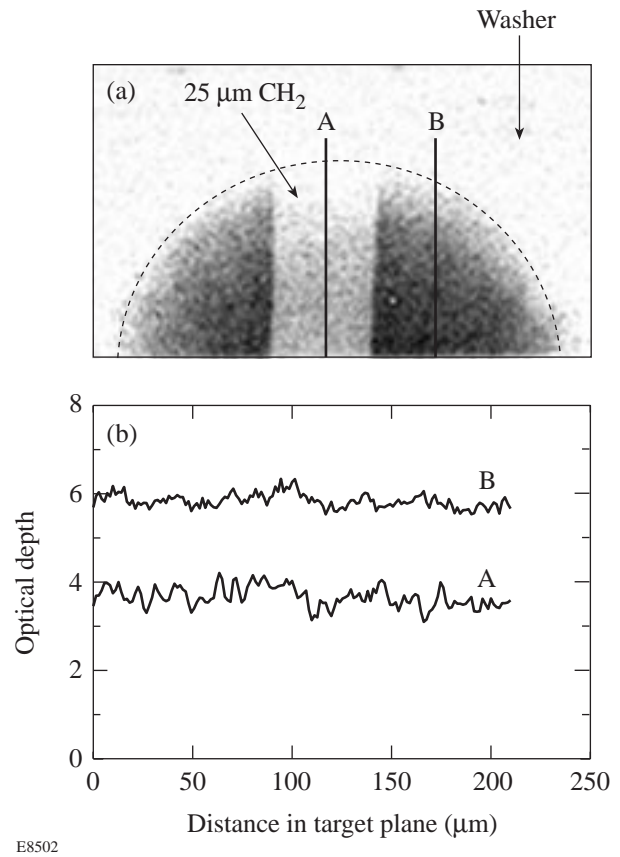
Figure 76.37
(a) Image of the undriven strip target; (b) lineouts of the measured optical depth (shown by lines A and B). Images through both the CH and open areas allow the optical depth to be measured.

line is the measured light intensity propagated through the system (and averaged in the direction parallel to the slit), and the thick solid line is the fit to experimental data assuming the framing camera MTF as a two-Gaussian function:

$$M_2(f) = 1.05 \exp\left\{-\left[103.8(\mu m)f\right]^2\right\}$$
$$-0.05 \exp\left\{-\left[95.8(\mu m)f\right]^2\right\}. \quad (14)$$

The measured MTF of the framing camera is shown in Fig. 76.40. This MTF is similar to that measured in other experiments performed at LLNL[11,12] and NRL[13] with aluminized phosphor plates, which have reduced the long-scale-length scattering of photons and electrons between the phosphor

and microchannel plates. This scattering resulted in a reduction of the MCP resolution up to about 20% at low spatial frequencies < 5 mm^{-1}. In our experiments, the phosphor plate was not aluminized. We saw, however, no significant reduction of the MTF at low spatial frequencies due to such scattering because of much lower levels of irradiation, compared with above-mentioned experiments.

Figure 76.41 shows the various MTF's discussed above. The thin solid line is the MTF of the entire system as determined by its edge response. The dotted line is the system MTF calculated as the product of the MTF's of the 8-μm pinhole (dot–dashed line), the framing camera (dashed line), and the 20-μm digitizing aperture (thick solid line). These MTF's assumed a system magnification of ~14. It can be seen that for
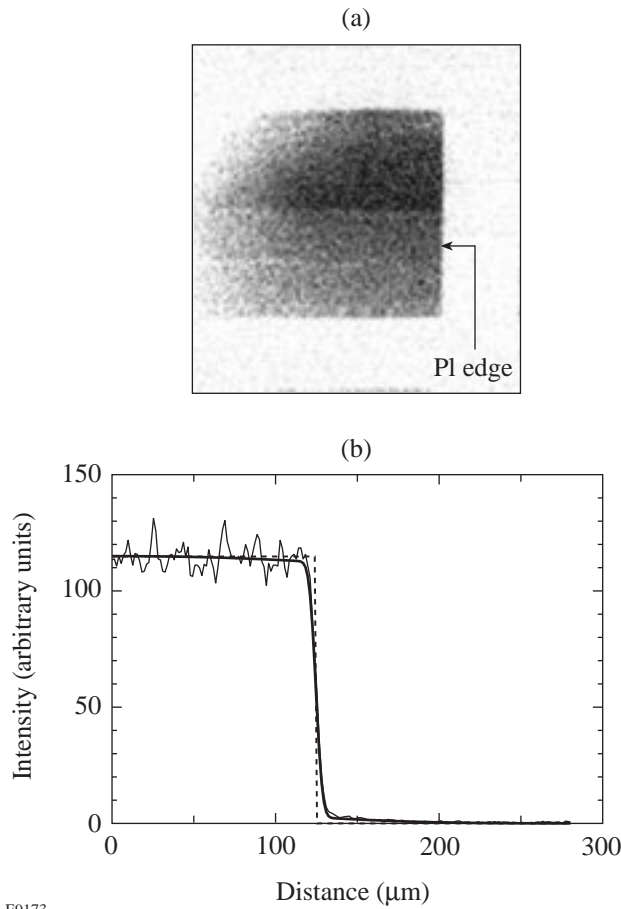
Figure 76.38
(a) Image of the edge target (Pt strip). (b) The dashed line represents the light intensity incident on the edge. The thin solid line is the measured light intensity propagated through the system (and averaged in the direction parallel to the edge), and the thick solid line is the fit to experimental data, assuming the system MTF to be a two-Gaussian function.
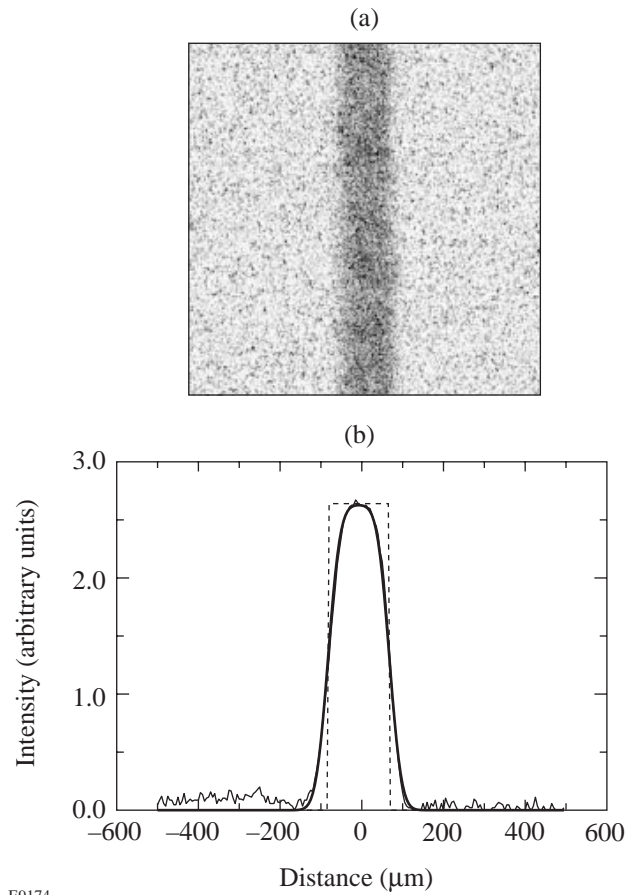
Figure 76.39
(a) Image of the slit target, installed in front of the MCP. (b) The dashed line represents the light intensity incident on the slit, the thin solid line is the measured light intensity propagated through the system (and averaged in the direction parallel to the slit), and the thick solid line is the fit to experimental data, assuming the framing-camera MTF to be a two-Gaussian function.

spatial frequencies below 70 mm^{-1}, the measured system MTF is in reasonable agreement with the aggregate response of the individual components. So in the analysis of target nonuniformity evolution (discussed in the **Wiener Filtering** section), we analyzed the signal only at frequencies below 70 mm^{-1}.

System Noise

Using radiographs of strip targets [see Fig. 76.37(a)], the system noise was characterized. Since the strip targets were uniform with very smooth surfaces, all nonuniformity measured in the radiographs of these targets is noise. The primary noise sources in this system are photon statistical noise of backlighter x rays, noise in the microchannel (MCP) and phosphor plates, film noise, and noise produced during digiti-
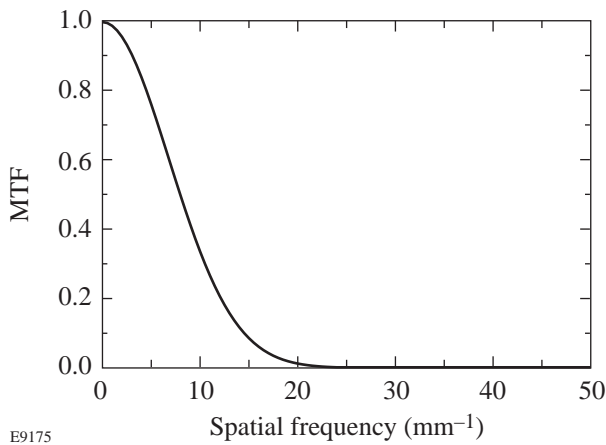
Figure 76.40
Resolution of the framing camera.
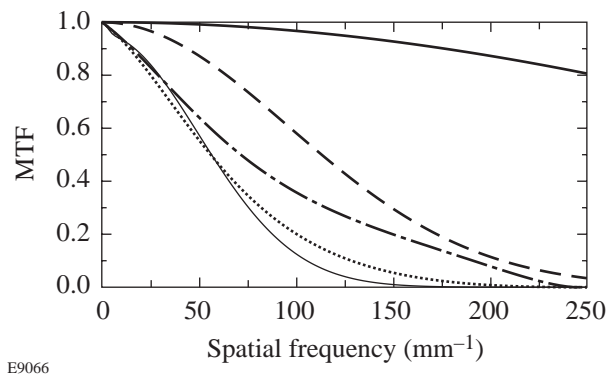
Figure 76.41
Resolution of the system. The thin solid line is the measured MTF of the entire system. The dotted line is the system MTF calculated as the product of the MTF's of the 8-μm pinhole (dot–dashed line), the framing camera (dashed line), and the 20-μm digitizing aperture (thick solid line).

zation. It is possible to determine the origin of noise based on its spectrum since, in frequency space, the signal and noise at each stage are multiplied by the MTF of that portion of the system.

Figure 76.42 depicts the azimuthally averaged Fourier amplitudes of the optical depth for two square regions with 150-μm width, through and around the strip. At high frequencies (>100 mm^{-1}), the averaged noise is nearly constant, indicative of the noise from film and digitization. At lower spatial frequencies the noise amplitude depends on the MTF's of the pinhole camera and MCP. This suggests that the dominant noise source is the photon statistics of the backlighter x rays. In optical-depth space, the noise amplitude is inversely proportional to the square root of the number of photons. There is more noise in the region of the strip with few x-ray photons than in the region out of the strip.

This relationship between noise levels and the photon flux can be explained by the following consideration: If I_1 and I_2 are the average x-ray intensities in and out of the strip regions, respectively, then noise rms amplitudes in these regions are ~ $\sqrt{I_1}$ and $\sqrt{I_2}$, assuming a monochromatic x-ray spectrum. Since the signal's optical depth is the natural logarithm of its intensity, the variation of a signal from its averaged value in terms of the optical depth will be proportional to $1/\sqrt{I_1}$ and $1/\sqrt{I_2}$ after a series expansion of the logarithm, retaining only the first term. It is assumed that the number of x-ray photons per pixel is greater than 1, which is necessary to justify such an analysis. The fact that there is more noise in the optical depth in the attenuated strip region with fewer x-ray photons (rms
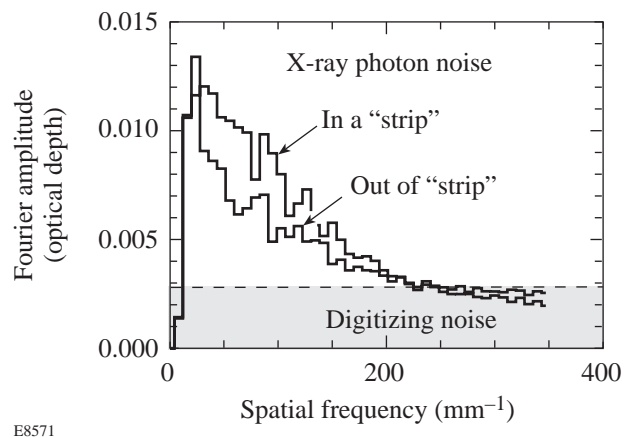
Figure 76.42
System noise. The measured noise level for two portions of a radiograph through and around the 25-μm-CH$_2$ strip target.

amplitude $\sim 1/\sqrt{I_1}$) than in the region out of the strip (rms amplitude $\sim 1/\sqrt{I_2}$) supports the suggestion of the photon-statistical nature of the noise.

Wiener Filtering

Using the measured system sensitivity, resolution, and noise, we recovered the imprinted perturbations from the radiographic images. A broad spectrum of imprinted features has been generated by laser nonuniformities with spatial frequencies up to 430 mm^{-1}. These initial imprinted nonuniformities in our experiments come from the nonuniformities in drive-laser beams used with distributed phase plates (DPP's).[14] The RT instability has growth rates and saturation effects that depend upon spatial frequency. In addition, the resolution of the radiographic system begins to cut off spatial frequencies above ~70 mm^{-1}. As a result, the detected signal resides in a narrow range of spatial frequencies ~10 to 70 mm^{-1}.

We analyzed 400-μm-square sections of the radiographic images of the target by converting them to measured optical depth, compensating for the backlighter envelope using a fourth-order, two-dimensional polynomial fit. The signal non-uniformity is expressed as the power per mode in optical depth by Fourier transforming the resulting optical depth.

A Wiener filter was developed to recover the true signal from the resulting images.[15] If $C(\mathbf{f})$ is the signal plus noise measured by the system, $C(\mathbf{f}) = S(\mathbf{f}) + N(\mathbf{f})$, then the restored signal $P(\mathbf{f})$ is

$$P(\mathbf{f}) = \frac{C(\mathbf{f})}{M_{\text{sys}}} \frac{|S(\mathbf{f})|^2}{|S(\mathbf{f})|^2 + |N_{\text{avg}}(\mathbf{f})|^2}, \qquad (15)$$

where M_{sys} is total system MTF, $|N_{\text{avg}}(\mathbf{f})|^2$ is the average or Wiener noise spectrum, and $|S(\mathbf{f})|^2$ is the measured signal power spectrum. The average noise spectrum $|N_{\text{avg}}(\mathbf{f})|^2$ and system MTF have been measured as described above; the only unknown is $|S(\mathbf{f})|^2$, the measured signal power spectrum. In this technique, the signal is compared to the measured noise spectrum, and only points that are greater than twice the amplitude of that noise are considered first, i.e.,

$$|S(\mathbf{f})|^2 = |C(\mathbf{f})|^2 - |N_{\text{avg}}(\mathbf{f})|^2,$$

for $\qquad\qquad\qquad\qquad\qquad\qquad\qquad\qquad (16)$

$$|C_{\text{re}}(\mathbf{f})| \text{ or } |C_{\text{im}}(\mathbf{f})| > 2|N_{\text{avg}}(\mathbf{f})|,$$

where $|C_{\text{re}}(\mathbf{f})|$ and $|C_{\text{im}}(\mathbf{f})|$ are real and imaginary parts of the measured signal with noise. Due to the statistical nature of the noise spectrum, the signal that is less than twice the noise amplitude can be treated in three primary manners: (a) rejected (i.e., set to 0), (b) considered to be uniformly distributed between zero and twice the noise level, or (c) set equal to twice the noise level. These options are used to provide the uncertainties of the measured signal. At higher spatial frequencies (>70 mm^{-1}) the detector response is falling rapidly, so the signal-to-noise level is greatly reduced and the error bars are larger.

The thin solid line in Fig. 76.43(a) shows the power per mode of the noise. The thick solid line represents the power per mode of the image at ~2 ns. These two lines are almost the same at high spatial frequencies > 80 mm^{-1}, suggesting that the

E9176
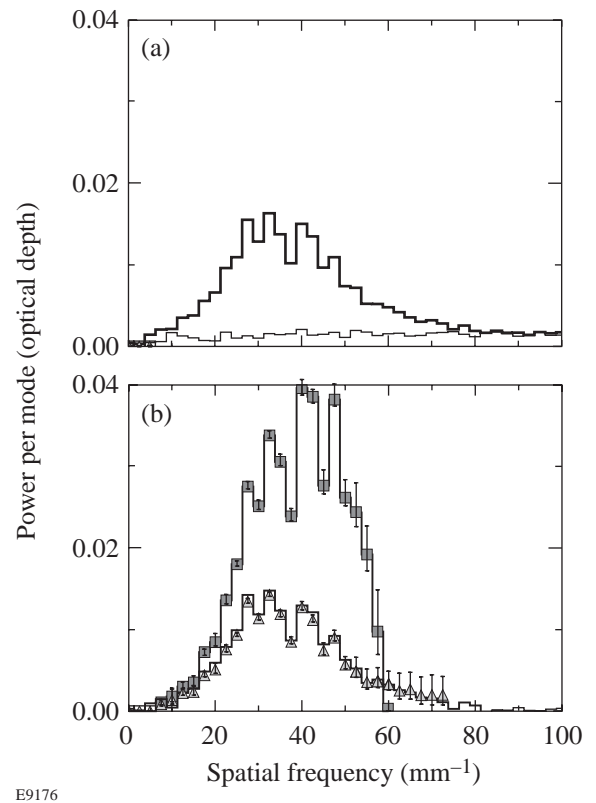
Figure 76.43
(a) Power per mode of the noise (thin solid line) and power per mode of the signal plus noise of the driven foil image at 2 ns. (b) Power per mode of target modulations versus spatial frequency. This is calculated using a Wiener filter, assuming MTF = 1 (triangles), calculated by subtracting the noise power per mode from the power per mode of the signal plus noise (lower solid line that agrees with triangles), and calculated using a Wiener filter, assuming a measured MTF (squares).

noise dominates at these spatial frequencies in the 2-ns image. There is a significant level of signal at lower spatial frequencies, however, which must be separated from noise.

The result of the Wiener filter[15] is shown in Fig. 76.43(b). To demonstrate the effect of noise reduction, we set the MTF = 1 (i.e., no resolution compensation) in Eq. (15); this is shown as the triangles in Fig. 76.43(b). The lower solid line shows the data obtained by simply subtracting the noise power per mode [the thin solid line in Fig. 76.43(a)] from the measured power per mode of signal plus noise [the thick solid line in Fig. 76.43(a)]. The agreement between these curves indicates that the noise compensation portion of the Wiener filter behaves reasonably. The upper curve in Fig. 76.43(b) depicts the result using the proper MTF and represents the fully processed data used as our experimental results.

Conclusions

By properly characterizing our detection system, we have simplified the complex relation between radiographic images and the optical depth in the target. Using measured aspects of the system, we have generated linear approximations of the system response that apply to our conditions. We measured the sensitivity and the resolution and demonstrated that they remain constant for the duration of the experiment. Using measured noise spectra, we have constructed a Wiener filter that enables us to distinguish the signal from noise and to reconstruct that signal by deconvolving system MTF. This technique is routinely applied to the analysis of our experiments.

REFERENCES

1. D. K. Bradley, J. A. Delettrez, R. Epstein, R. P. J. Town, C. P. Verdon, B. Yaakobi, S. Regan, F. J. Marshall, T. R. Boehly, J. P. Knauer, D. D. Meyerhofer, V. A. Smalyuk, W. Seka, D. A. Haynes, Jr., M. Gunderson, G. Junkel, C. F. Hooper, Jr., P. M. Bell, T. J. Ognibene, and R. A. Lerche, Phys. Plasmas **5**, 1870 (1998).

2. S. G. Glendinning *et al.*, in *Applications of Laser Plasma Radiation II*, edited by M. C. Richardson and G. A. Kyrala (SPIE, Bellingham, WA, 1995), Vol. 2523, pp. 29–39.

3. T. R. Boehly, V. A. Smalyuk, D. D. Meyerhofer, J. P. Knauer, D. K. Bradley, C. P. Verdon, and D. Kalantar, in *Laser Interaction and Related Plasma Phenomena*, edited by G. H. Miley and E. M. Campbell (American Institute of Physics, New York, 1997), Vol. 406, pp. 122–129.

4. J. P. Knauer, C. P. Verdon, D. D. Meyerhofer, T. R. Boehly, D. K. Bradley, V. A. Smalyuk, D. Ofer, P. W. McKenty, S. G. Glendinning, D. H. Kalantar, R. G. Watt, P. L. Gobby, O. Willi, and R. J. Taylor, in *Laser Interaction and Related Plasma Phenomena*, edited by G. H. Miley and E. M. Campbell (American Institute of Physics, New York, 1997), Vol. 406, pp. 284–293.

5. T. Endo *et al.*, Phys. Rev. Lett. **74**, 3608 (1995).

6. R. Ishizaki and K. Nishihara, Phys. Rev. Lett. **78**, 1920 (1997).

7. D. H. Kalantar, M. H. Key, L. B. Da Silva, S. G. Glendinning, B. A. Remington, J. E. Rothenberg, F. Weber, S. V. Weber, E. Wolfrum, N. S. Kim, D. Neely, J. Zhang, J. S. Wark, A. Demir, J. Lin, R. Smith, G. J. Tallents, C. L. S. Lewis, A. MacPhee, J. Warwick, and J. P. Knauer, Phys. Plasmas **4**, 1985 (1997).

8. B. A. Remington *et al.*, Phys. Fluids B **4**, 967 (1992).

9. An earlier version of *LILAC* is described in E. Goldman, Laboratory for Laser Energetics Report No. 16, University of Rochester (1973).

10. B. A. Remington *et al.*, Rev. Sci. Instrum. **63**, 5080 (1992).

11. J. D. Wiedwald *et al.*, in *Ultrahigh- and High-Speed Photography, Videography, Photonics, and Velocimetry '90*, edited by L. L. Shaw, P. A. Jaanimagi, and B. T. Neyer (SPIE, Bellingham, WA, 1990), Vol. 1346, pp. 449–455.

12. H. F. Robey, K. S. Budil, and B. A. Remington, Rev. Sci. Instrum. **68**, 792 (1997).

13. C. J. Pawley, A. V. Deniz, and T. Lehecka "Noise and Sensitivity in X-Ray Framing Cameras," to be published in the Review of Scientific Instruments.

14. Y. Lin, T. J. Kessler, and G. N. Lawrence, Opt. Lett. **20**, 764 (1995).

15. L. R. Rabiner and B. Gold, *Theory and Application of Digital Signal Processing* (Prentice-Hall, Englewood Cliffs, NJ, 1975).